

# High-Speed Coherent Raman Fingerprint Imaging of Biological Tissues

Charles H. Camp Jr.,<sup>1</sup> Young Jong Lee,<sup>1</sup> John M. Heddleston,<sup>2</sup> Christopher M. Hartshorn,<sup>1</sup>  
Angela R. Hight Walker,<sup>2</sup> Jeremy N. Rich,<sup>3</sup> Justin D. Lathia,<sup>4</sup> and Marcus T. Cicerone<sup>1,\*</sup>

<sup>1</sup>*Biosystems and Biomaterials Division, National Institute of Standards  
and Technology, 100 Bureau Dr, Gaithersburg, MD 20899, USA*

<sup>2</sup>*Semiconductor and Dimensional Metrology Division,  
National Institute of Standards and Technology, 100 Bureau Dr, Gaithersburg, MD 20899, USA*

<sup>3</sup>*Department of Stem Cell Biology and Regenerative Medicine,  
Cleveland Clinic, 9500 Euclid Ave, Cleveland, OH 44195, USA*

<sup>4</sup>*Department of Cellular and Molecular Medicine,  
Cleveland Clinic, 9500 Euclid Ave, Cleveland, OH 44195, USA*

An imaging platform based on broadband coherent anti-Stokes Raman scattering (BCARS) has been developed which provides an advantageous combination of speed, sensitivity and spectral breadth. The system utilizes a configuration of laser sources that probes the entire biologically-relevant Raman window ( $500\text{ cm}^{-1}$  to  $3500\text{ cm}^{-1}$ ) with high resolution ( $< 10\text{ cm}^{-1}$ ). It strongly and efficiently stimulates Raman transitions within the typically weak “fingerprint” region using intrapulse 3-colour excitation, and utilizes the nonresonant background (NRB) to heterodyne amplify weak Raman signals. We demonstrate high-speed chemical imaging in two- and three-dimensional views of healthy murine liver and pancreas tissues and interfaces between xenograft brain tumours and the surrounding healthy brain matter.

## Introduction

Raman spectroscopy is a powerful label-free technique for analyzing the chemical species within biological samples. It has been extensively applied to a variety of tissue types and pathologies<sup>1–3</sup> providing a high degree sensitivity and specificity. In these and similar studies<sup>4–8</sup>, multiple peaks within the weakly scattering Raman fingerprint region ( $< 1,800\text{ cm}^{-1}$ ) are used to discriminate subtly different states of cells and tissues. Until now, fingerprint spectra of sufficient quality for such studies have only been available with collection times ranging (0.2 to 30) seconds<sup>4–8</sup>, seriously limiting its use in high-resolution imaging that is critical for widespread adoption in biological research and clinical practice. To bolster the inherently weak Raman scattering process, coherent Raman imaging (CRI) techniques have been developed that coherently populate selected vibrational states of molecules through their nonlinear response to multiple pulsed laser fields.

Narrowband CRI techniques, such as coherent anti-Stokes Raman scattering (CARS)<sup>9</sup> and stimulated Raman scattering (SRS)<sup>10,11</sup>, are capable of video-rate imaging of single Raman bands<sup>12,13</sup>, but suffer from limitations in breadth and speed of laser tuning rates. CARS, specifically, is also limited by a nonresonant background (NRB) that distorts the Raman signal through coherent mixing and seriously limits Raman peak identification without scanning over a wide spectral range. The net effect limits narrowband CARS to species with high oscillator density and uniquely isolated Raman peaks, essentially preventing access to the chemically rich fingerprint region.

Multiplex techniques, such as multiplex SRS<sup>14–18</sup> and BCARS<sup>19–22</sup>, provide an alternative stimulation profile in which multiple Raman transitions are probed simultaneously. Multiplex SRS is free of NRB, but it is currently limited by small bandwidths<sup>14,16,17</sup>, pulse shaping rates<sup>17,18</sup>, coarse spectral resolution<sup>17</sup>, and competing nonlinear phenomena<sup>23</sup>. The BCARS signal is accompanied by an NRB, but, because it is a spectroscopic technique, it can be performed in a manner such that the NRB is used as a heterodyne amplifier for weak Raman peaks<sup>24</sup>, and NRB-induced spectral distortions are removed numerically<sup>25–27</sup>, but it, too, has been hampered by several challenges. BCARS techniques are capable of probing over  $3000\text{ cm}^{-1}$ , but inefficiently stimulate Raman transitions through 2-colour excitation (described below) that limits spectral detection in biological samples to just the CH-/OH-stretch region and the strongest few fingerprint peaks with (30 - 300) ms dwell times<sup>28,29</sup>. Intrapulse CARS techniques use a 3-colour excitation mechanism (also described below) to address primarily the fingerprint region, but, thus far, have been limited to fingerprint imaging of only strongly scattering systems such as neat liquids and polymer films<sup>30,31</sup>.

In this work, we present a BCARS system that efficiently stimulates Raman transitions, especially within the weak fingerprint region, using intrapulse 3-colour excitation, and exploits the strong NRB for amplifying the inherently weak

---

\*Electronic address: [cicerone@nist.gov](mailto:cicerone@nist.gov)

fingerprint signal. The combination of these two features allows us to record spectra one to two orders-of-magnitude faster than previously possible and with high spectral clarity, paving a way toward CRI integration into widespread biological and clinical use.

## Results

### System Design

Figure 1a presents a schematic of the BCARS system, which uses tailored co-seeded fiber lasers to generate a narrowband flat-top probe (770 nm;  $\approx 16$  mW, 3.4 ps on-sample) and a supercontinuum (SC) ( $\sim 900$  nm to 1,350 nm;  $\approx 9.5$  mW,  $\approx 16$  fs pulses on-sample) with negligible jitter, a similar laser design to Selm *et al.*<sup>32</sup>. This particular configuration provides an independent, robust probe source for high-resolution spectra ( $< 10$   $\text{cm}^{-1}$ ); stimulates the fingerprint region using intrapulse 3-colour excitation, which is particularly strong, efficient, and maximal at the lowest energy levels; and stimulates higher energy transitions using 2-colour excitation; thus, accessing the entire biologically-relevant Raman window ( $\sim 500$ -3500  $\text{cm}^{-1}$ ). We avoid NRB-reduction schemes so as to maximally generate the resonant signal and the nonresonant signal for heterodyne amplification.

The developed system uses two different excitation methods. These mechanisms operate simultaneously as they are simply different permutations of the same two pulses, but their properties differ significantly. To illustrate this, we begin with an expression for the frequency-domain CARS signal intensity,  $I_{\text{CARS}}(\omega)$ :

$$I_{\text{CARS}}(\omega) \propto \left| \left\{ \chi^{(3)}(\omega) [E_S(\omega) \star E_p(\omega)] \right\} * E_{pr}(\omega) \right|^2 \quad (1)$$

where  $\omega$  is frequency,  $\chi^{(3)}$  is the 3rd-order nonlinear susceptibility,  $E_p$ ,  $E_s$ , and  $E_{pr}$  are the pump, Stokes, and probe fields, respectively, and  $\star$  and  $*$  are the cross-correlation and convolution operators, respectively. The term in square brackets is the frequency-domain coherence generation profile, which will maximize at the frequency difference between the peaks of the pump and Stokes fields. Assuming real, Gaussian fields, the integrated spectral intensity over all frequencies is given as:

$$\langle I_{\text{CARS}} \rangle \propto \mathcal{P}_p \mathcal{P}_S \mathcal{P}_{pr} \frac{\sigma_p \sigma_S \sigma_{pr}}{\sqrt{\sigma_p^2 + \sigma_S^2 + \sigma_{pr}^2}} \quad (2)$$

where  $\mathcal{P}_p$ ,  $\mathcal{P}_S$ , and  $\mathcal{P}_{pr}$  are the pump, Stokes, and probe spectrally integrated modulus-squared field (proportional to average power), such that  $\mathcal{P} = \langle |E|^2 \rangle = |E_0|^2 \sqrt{\pi} \sigma$ , where  $E_0$  is the field envelope amplitude with  $1/e$  half-width  $\sigma$ .

Under “2-colour” (2C) excitation (Figure 1b), used in BCARS/MCARS systems with degenerate pump and probe sources<sup>19–22</sup> ( $\mathcal{P}_{p,pr} \equiv \mathcal{P}_p = \mathcal{P}_{pr}$ ;  $\sigma_{p,pr} \equiv \sigma_p = \sigma_{pr}$ ), the BCARS signal resolution is provided by the narrowband pump-probe source, and the spectral breadth is provided by the Stokes source; thus, from (2):

$$\langle I_{2C} \rangle \propto \mathcal{P}_{p,pr}^2 \mathcal{P}_S \frac{\sigma_{p,pr}^2 \sigma_S}{\sqrt{2\sigma_{p,pr}^2 + \sigma_S^2}} \approx \mathcal{P}_{p,pr}^2 \mathcal{P}_S \sigma_{p,pr}^2. \quad (3)$$

For intrapulse “3-colour” (3C) excitation (Figure 1c) in which the probe is independent and the SC provides the pump and Stokes photons ( $\mathcal{P}_{p,S} \equiv \mathcal{P}_p = \mathcal{P}_S$ ;  $\sigma_{p,S} \equiv \sigma_p = \sigma_S$ ):

$$\langle I_{3C} \rangle \propto \mathcal{P}_{p,S}^2 \mathcal{P}_{pr} \frac{\sigma_{p,S}^2 \sigma_{pr}}{\sqrt{2\sigma_{p,S}^2 + \sigma_{pr}^2}} \approx \mathcal{P}_{p,S}^2 \mathcal{P}_{pr} \sigma_{p,S} \sigma_{pr}. \quad (4)$$

We note two important differences between these coherence generation mechanisms. One is that the 2-colour mechanism has a peak excitation profile at the difference frequency between the narrowband and SC pulses (near 2800  $\text{cm}^{-1}$  for our system), whereas the intrapulse 3-colour mechanism has a peak excitation frequency at 0  $\text{cm}^{-1}$ , since the pump and Stokes fields are degenerate. Thus, the former excites the CH-/OH-stretch region that typically presents an intrinsically stronger response, whereas the latter excites the fingerprint region with the weaker intrinsic response. The other important difference in these mechanisms is their efficiency over a broad bandwidth. For 2-colour excitation, as described in (3), the total CARS signal is independent of the Stokes source bandwidth,  $\sigma_S$ . Thus with increasing  $\sigma_S$ , the total integrated CARS signal remains constant, but the signal at each spectral increment will decrease. In contrast, as described in (4), the total 3-colour CARS signal rises with increasing bandwidth,  $\sigma_{p,S}$ . Importantly, the

signal at each spectral increment also increases with increasing  $\sigma_{p,S}$ . From this comparison, one can appreciate that the 3-colour mechanism is much more efficient than the 2-colour mechanism for the present system. We can quantify the relative efficiency as:  $\langle I_{3C} \rangle / \langle I_{2C} \rangle \propto \sigma_S / \sigma_{pr} \approx 100$ ; thus, this system provides strong and efficient excitation where it is most needed within the fingerprint region. A more thorough treatment of these topics is presented in the Supplementary Information section ‘2-Colour and 3-Colour Excitation Methods’.

Utilizing 3-colour generation is necessary, but not sufficient to achieve the required signal levels within the fingerprint region. CARS imaging with 3-colour excitation was first reported more than 10 years ago<sup>31</sup>, but until now has been limited to fingerprint imaging of only strongly scattering systems such as neat liquids and polymer films<sup>30,31</sup>. To best take advantage of the strong 3-colour stimulation, requires the full utilization of the NRB. Without the heterodyne amplification provided by the NRB, our signal-to-noise ratio (SNR) at high-speed acquisition would be less than 1 for most Raman fingerprint peaks. As previously described, the NRB limits the vibrational sensitivity and specificity of narrowband CARS techniques<sup>9,24</sup>, however, it acts as a robust local oscillator for heterodyne amplification of the resonant signal when spectral phase retrieval is applied numerically after the signal is collected<sup>25,26</sup>. This amplification can bring the weaker Raman peaks above the noise floor, increasing their effective SNR by over an order of magnitude (see Supplementary Information section ‘Nonresonant Background as Heterodyne Amplifier’).

The spectra generated by this combination of 2-colour and 3-colour excitation are collected with a spectrometer equipped with a thermoelectrically cooled charged-coupled device (CCD) camera that affords acquisition times down to 3.5 ms per spectrum. Our spectrometer detection range is sufficiently broad ( $> 250$  nm) to acquire signal from BCARS as well as other nonlinear processes, such as second-harmonic generation (SHG) and two-photon excited fluorescence (TPEF), providing an additional layer of information for BCARS spectral interpretation. Figure 1d shows a raw BCARS spectrum of 99 % glycerol (acquisition time: 3.5 ms; SNR: 15 dB to 23 dB), which shows the intense 3-colour response in the range ( $\approx 425$  to  $2,000$ )  $\text{cm}^{-1}$  that dwarfs the 2-colour response ( $\approx 2,000$  to  $3,600$ )  $\text{cm}^{-1}$ . Although the raw BCARS spectrum is distorted due to coherent mixing between the resonant CARS signal and the NRB<sup>9</sup>, Figure 1e demonstrates the use of a time-domain Kramers-Kronig (TDKK) transform to retrieve the imaginary component of the nonlinear susceptibility<sup>25</sup>,  $\Im\{\chi^{(3)}\}$  (convolved with the probe source spectral profile), that is proportional to the [spontaneous] Raman response of the molecule. See the Supplementary Information section ‘Spontaneous and Coherent Raman Spectroscopy of Glycerol’ demonstrating the significant speed enhancement. We use the TDKK for its speed advantage over competing techniques<sup>27</sup>. To examine the detection limit of the BCARS system and demonstrate molecular response linearity, we recorded spectra from a methanol-water dilution series (time-averaged over 1 second<sup>10</sup>). As shown in Figure 1f, the response of the retrieved  $\Im\{\chi^{(3)}\}$  is linear with respect to methanol concentration (starting from 1 mol/L; zoomed-in for clarity), and the detection limit of the system was determined to be  $< 23$  mmol/L using the C-O stretch peak at  $\approx 1,037$   $\text{cm}^{-1}$  and  $< 8$  mmol/L using the C-H stretch peak at  $\approx 2,839$   $\text{cm}^{-1}$ , which matches closely with similar SRS measurements<sup>10</sup>.

### Tissue Imaging

To date, histological analysis of tissues using CRI has relied on limited spectral information primarily in the strong CH-/OH-stretch region of the Raman spectrum ( $\approx 2,700$   $\text{cm}^{-1}$  to  $3,500$   $\text{cm}^{-1}$ )<sup>12,17,28,33</sup>. With these limitations and the complexity of tissue specimens, spectrally identifying even such common features as nuclei are nontrivial tasks. To demonstrate the sensitivity of the present CRI system using molecular fingerprint signatures, we imaged murine liver tissue sections. Figure 2a shows a pseudocolour image of liver tissue near a portal triad (hepatic artery, hepatic portal vein, and bile duct) that was collected with 3.5 ms dwell times over a  $200 \mu\text{m} \times 200 \mu\text{m}$  area ( $300 \text{ pixels} \times 300 \text{ pixels}$ ). This image contrasts nuclei in blue based on the Raman band  $\approx 785$   $\text{cm}^{-1}$ , which emanates from DNA/RNA pyrimidine ring breathing and the phosphodiester-stretch<sup>34</sup>. For further chemical contrast or specificity, one could use other nucleotide peaks at (668, 678, 728, 750, 829, 1,093, 1,488, and 1,580)  $\text{cm}^{-1}$ . Additionally, the peak at 830  $\text{cm}^{-1}$  could be used to gauge the amount of DNA in the B-conformation relative to the total genetic content providing information about the functional state of the cells. As a general protein contrast, the ring breathing contribution of phenylalanine at 1,004  $\text{cm}^{-1}$  is presented in green. The collagen is highlighted in red using the 855  $\text{cm}^{-1}$  C-C-stretch from the pyrrolidine ring of proline (C-C-stretch at 938  $\text{cm}^{-1}$  also provides similar contrast<sup>35</sup>). Previous CRI investigations of tissue incorporated SHG and TPEF imaging to identify collagen and elastin, respectively<sup>4,36</sup>, which is shown in Figure 2b, with demonstrative spectra in Figure 2c. It should be noted, however, that SHG and TPEF provide uncertain chemical specificity as other biologically-relevant molecular species are known to generate a response as well<sup>37</sup>. Additionally, we note that Raman and SHG present differing contrasts of collagen as Raman (and by extension, BCARS) is sensitive to molecular structure<sup>35,38</sup> while SHG is sensitive to supermolecular crystalline structure<sup>39–41</sup>.

With this level of spatial resolution and chemical contrast, several hepatic structures are identifiable by their histology: the hepatic artery with its circular protein-rich, collagen-poor band (likely smooth muscle) surrounding a

thin endothelial layer and lumen, the bile ducts lined by tightly packed cuboidal epithelial cells, and the relatively large portal vein with its sparse (due to microtome sample preparation) endothelial layer. Additionally one can see the connective tissue septa (primarily collagen) that enmeshes the portal triad.

Although the pseudocolour image in Figure 2a is limited to 3 colours, which are presented in high-contrast grayscale in Figures 2d-f, one can identify significant spectral complexity in the sample as illustrated by the single-pixel spectra in Figure 2g. Using isolated peaks, one could create dozens of unique images based on vibrational susceptibilities, such as those shown in Figures 2h-k:  $1,302\text{ cm}^{-1}$  ( $\text{CH}_2$ -deformation),  $1,665\text{ cm}^{-1}$  (Amide I/ $\text{C}=\text{C}$ -stretch),  $2,884\text{ cm}^{-1}$  ( $\text{CH}_2$ -stretch),  $3,228\text{ cm}^{-1}$  (O-H-stretch), respectively. Additionally, multivariate analysis of contributions from several peaks, their locations, intensities, and shapes present significant avenues of chemical contrast. For example, Figure 2l highlights elastin by segmenting the chemical species that have vibrations at  $(1,126\text{ and }1,030)\text{ cm}^{-1}$  but lack vibrations at  $(677, 817, \text{ and }1,302)\text{ cm}^{-1}$ , which isolates elastin from collagen and other proteins, lipids, and nucleotides<sup>35</sup>. Similarities and differences between the BCARS image and the TPEF image in Figure 2b, indicate that although elastin is the most abundant fluorescent molecule, multiple chemical species contribute to the TPEF signal<sup>37</sup>.

Beyond histochemical imaging in two dimensions, nonlinear excitation in CARS makes it an intrinsically sectioning microscopy, affording the generation of “z-stack” images in three dimensions. Narrowband CARS and SRS have demonstrated this capability<sup>9,11,13,33</sup>, but three-dimensional microspectroscopy with BCARS or spontaneous Raman has been uncommon due to long acquisition times. Figure 3a is a BCARS image of murine pancreas highlighting the nuclei in blue ( $785\text{ cm}^{-1}$ ), collagen in red ( $855\text{ cm}^{-1}$ ), and a general contrast for lipids and protein in green ( $1,665\text{ cm}^{-1}$ : lipids,  $\text{C}=\text{C}$ -stretch; proteins, Amide I). This image shows a single plane from a 10-stack collection with each plane covering  $150\text{ }\mu\text{m} \times 100\text{ }\mu\text{m}$  ( $0.667\text{ }\mu\text{m}$  lateral,  $1\text{ }\mu\text{m}$  axial step size;  $< 2$  minutes per image). Additionally, two reconstructed axial planes are shown. This image shows an interlobular exocrine duct surrounded by epithelial cells, the edge of a larger interlobular exocrine duct (as identified by the columnar epithelial cells), a collagen matrix, and acinar cells (and the lumen separating the acini). Figure 3b shows the reconstructed 3D image that more clearly shows the shape, size, and orientation of the individual cells and tissue constituents. Figure 3c shows single pixel spectra from the nucleus of an epithelial cell, collagen, and from the cytosol of an acinar cell.

For histopathological analysis, spontaneous Raman and infrared micro/spectroscopy have demonstrated adequate chemical specificity and sensitivity to delineate a variety of neoplasms<sup>1-8,42</sup>, but required long integration times and presented coarse spatial resolution, which may limit accurate tumour-boundary identification and early-stage tumour detection. Conversely, CRI techniques have demonstrated high-speed, high-spatial resolution imaging of normal and diseased brain tissue but with contrast limited to single or few Raman peaks<sup>4,28,42</sup>. We present images of orthotopic xenograft brain tumours (see Methods for more detail) within a murine brain. Figure 4a shows a brightfield image of a brain slice ( $10\text{ }\mu\text{m}$  nominal thickness) with an identifiable tumour mass from which we imaged several areas (Figure 4b shows a close-up polarization micrograph of the specific imaging sites). Figure 4c shows a CRI image with nuclei in blue ( $730\text{ cm}^{-1}$ ), lipid-content in red ( $2,850\text{ cm}^{-1}$ ), and red blood cells in green ( $1,548\text{ cm}^{-1} + 1,565\text{ cm}^{-1}$ :  $\text{C}-\text{C}$ -stretch from hemoglobin<sup>43</sup>). This image clearly shows the large tumour mass and a projection of neoplastic cells within healthy tissue. Additionally, smaller tumour bodies are identifiable by their high density of distorted nuclei with high nuclear:cytoplasmic ratio. Figure 4d shows several small extensions of the main tumour mass invading healthy brain matter. The mesh-like appearance of the healthy tissue is likely an artifact of sectioning and the freeze-thaw cycle due to tissue density differences (see axial-scan in Figure 4d). Figure 4e shows the boundary between normal brain tissue (likely, gray matter), white matter, and tumour masses which contrasts lipids in red ( $2,850\text{ cm}^{-1}$ );  $\text{CH}_3$ -stretch -  $\text{CH}_2$ -stretch ( $2,944\text{ cm}^{-1} - 2,850\text{ cm}^{-1}$ ), a general contrast; and nuclei in blue ( $785\text{ cm}^{-1}$ ). The image shows the fibrous texture of white matter and strands of myelination around cancer cell clusters. Figure 4f shows single-pixel spectra from an intratumoural nucleus, the white matter, and normal brain. The spectra indicate lipids are most concentrated in the white matter and least in the tumour, which agrees with previous chromatographic<sup>44</sup> and vibrational spectroscopic studies<sup>6,45</sup>. Additionally, one sees an increase in response from phenylalanine ( $1,004\text{ cm}^{-1}$ ) and an overall reduction in the lipid-protein ratio in tumour cells relative to healthy brain tissues, both indicated in previous Raman studies<sup>42,45</sup>, but it was not established whether these changes manifested themselves across the tumour or in certain substructures. For further analysis, we spectrally segmented the tumour masses between intracellular regions and extracellular regions (Figure 4g). Figure 4h shows a histogram analysis of each pixel within the tumours indicating that the phenylalanine content is more concentrated within the nuclei, which is also indicated in the spectra in Figure 4i. Additionally the lipid-protein ratio ( $2,850\text{ cm}^{-1} / 1,004\text{ cm}^{-1}$ ) is largest in normal brain matter (14.5), weakest in the intranuclear tumoural space (6.9), and intermediate in the extranuclear tumoural space (12.8).

## Discussion

In this work, we have presented results from the development of a new CRI platform with an unprecedented combination of speed, sensitivity, and spectral breadth that has real potential to propel Raman imaging into widespread adoption in biological research and clinical use. Through the use of intrapulse 3-colour stimulation in conjunction with heterodyne amplification of the small Raman signal with the strong NRB, this system provides a level of signal clarity throughout the fingerprint region previously only available through spontaneous Raman but at speeds aligned with coherent Raman techniques. For demonstrative purposes, we presented BCARS images of healthy and neoplastic tissues that indicate that BCARS could be used to practically provide a new layer of information to researchers in conjunction with other molecular analysis techniques, such as antibody-based fluorescence staining, quantitative polymerase chain reaction (qPCR) or RNA sequencing microarray data.

In addition to the aforementioned biological investigations, there are a number of opportunities for improving the utility of the BCARS system. For example, advanced pulse shaping techniques could be implemented to tailor the excitation profile to particularly enhance the sensitivity over specific spectral ranges, such as the  $1,800\text{ cm}^{-1}$  to  $2,200\text{ cm}^{-1}$  range, for which our system currently has the least sensitivity. Additional hardware advances such as epidetection, as recently demonstrated<sup>46</sup>, could expand imaging to thick or opaque samples and in conjunction with endoscopy could provide an opportunity for *in vivo* imaging.

## Methods

Any mention of commercial products or services is for experimental clarity and does not signify an endorsement or recommendation by the National Institute of Standards and Technology.

### *BCARS Microscope*

The BCARS microspectrometer is constructed from two co-seeded fiber lasers (Toptica, FemtoPro) that provide attosecond-level synchronization with the narrowband probe laser generating  $\approx 3.4\text{ ps}$  flat-top pulses ( $\Delta\Omega < 10\text{ cm}^{-1}$ ) at  $770\text{ nm}$  (40 MHz repetition rate), and the SC source generating  $\approx 16\text{ fs}$  pulses (on-sample) spanning ( $\approx 900\text{ nm}$  to  $1,350\text{ nm}$ ) (40 MHz repetition rate). The SC beam is directed into an SF10 prism pair pulse compressor to provide a degree of chirp control as to maximize the spectral coherence window (additional laser tuning and higher-order chirp can move the 2- and 3-colour excitation regions to excite, for example, the Raman quiescent region when analyzing deuterated species or cyano groups). The probe beam is directed to a motorized optical delay line to provide temporal control between the two sources. Additionally, the probe beam size is enlarged by a refractive telescope to closely match the back aperture of the objective lens. The two beams are combined at a dichroic filter (Omega, 910DCSPXR) and coupled into an inverted microscope (Olympus, IX71). The excitation beams are focused onto the sample using a water-immersion,  $60\times$  ( $\text{NA} = 1.2$ ) objective lens (Olympus, UPlanSApo IR). The sample is mounted on a 3-axis piezo stage (Physik Instrumente, P-545) that provides  $200\text{ }\mu\text{m} \times 200\text{ }\mu\text{m} \times 200\text{ }\mu\text{m}$  movement with sub-micron precision. The excitation and generated photons are collected and collimated with a  $60\times$  objective lens ( $\text{NA} = 0.7$ ) (Olympus, LUCPlanFL N) and passed through two shortpass filters (Semrock, Brightline 770SP; Chroma, HHQ765SP). The remaining anti-Stokes light is focused with an achromatic lens onto the slit of a spectrograph (Acton, SpectroPro 2300i) that is equipped with a CCD camera (Andor, DU970N-FI) for spectral recording. With typical settings, each spectrum is recorded between  $\approx 470\text{ cm}^{-1}$  to  $3,800\text{ cm}^{-1}$  (full spectral range covers a larger region:  $\approx 268\text{ nm}$ ). The camera is directly synchronized with the piezo stage motion controller to allow constant-velocity raster scanning. Each fast-axis line scan is recorded onto the CCD on-board memory and transferred during slow-axis movement. The camera control and acquisition software and the data storage software were developed in-house using Visual C++ and controlled through a custom LabView (National Instruments) interface. The data is processed in MATLAB (Mathworks) through an in-house developed processing suite. Raw spectral data cubes are de-noised using singular value decomposition (SVD) (it should be noted that the average spectrum in Figure 4i was taken from data that was not de-noised with SVD as averaging effectively reduced the noise level without additional processing), a time-domain Kramers-Kronig transform (TDKK) for spectral phase retrieval<sup>25</sup>, and baseline detrended. For the TDKK, the estimated NRB signal was collected from either water or glass (slide or coverslip) with the probe delayed to the earliest overlap with the SC, a region in which the NRB dominates the resonant signal; thus, providing a good approximation to the pure NRB. Baseline detrending was performed by manually selecting local minima isolated from Raman peaks<sup>6</sup>. In the event that a sample shows regions of mounting media (water or PBS), the fingerprint region below  $1,600\text{ cm}^{-1}$  within these areas could be used as a model for the residual background and subtracted. All

pseudocolour images, vibrational images, and spectra were generated in MATLAB, and the 3D-reconstructed image in Figure 3b was generated in ImageJ (NIH).

### Tissue Sections

Fresh murine liver and pancreas tissues were commercially procured (Zyagen) pre-mounted on charged glass slides. The samples were shipped on dry ice and stored at  $-80^{\circ}\text{C}$ . Prior to imaging, the samples were thawed for 10 minutes, washed twice in PBS to remove debris and residual cutting media. The tissues were kept wet with PBS and a glass coverslip was placed over the sample and sealed with nail polish.

Glioblastoma cells (GCs) were isolated from primary surgical GBM biopsy specimens in accordance with protocols approved by the Duke University Medical Center or Cleveland Clinic Foundation Institutional Review Boards. *In vivo* tumour initiation studies were done with BALB/c nu/nu mice under a Cleveland Clinic Foundation Institutional Animal Care and Use Committee-approved protocol. All transplanted mice were maintained for 100 days or until development of neurologic signs, at which point they were euthanized by  $\text{CO}_2$  asphyxiation. Brains were removed and fixed in 4 % paraformaldehyde for 24 hours. Following fixation, brains were submerged in 30 % sucrose as cryoprotectant for an additional 24 hours. Samples were then frozen in optimal cutting temperature compound (OCT) and sectioned on a cryomicrotome to a nominal thickness of  $10\text{ }\mu\text{m}$ . Prior to imaging, samples were thawed, washed with PBS to remove OCT and debris, then covered with a glass coverslip and sealed with nail polish.

- 
- [1] Huang, Z. *et al.* Near-infrared Raman spectroscopy for optical diagnosis of lung cancer. *Int. J. Cancer* **107**, 1047–1052 (2003).
  - [2] Haka, A. S. *et al.* Diagnosing breast cancer by using Raman spectroscopy. *P. Natl. Acad. Sci. USA* **102**, 12371–12376 (2005).
  - [3] Gniadecka, M. *et al.* Melanoma diagnosis by Raman spectroscopy and neural networks: structure alterations in proteins and lipids in intact cancer tissue. *J. Invest. Dermatol.* **122**, 443–449 (2004).
  - [4] Meyer, T. *et al.* Nonlinear microscopy, infrared, and Raman microspectroscopy for brain tumor analysis. *J. Biomed. Opt.* **16**, 021113 (2011).
  - [5] Kirsch, M., Schackert, G., Salzer, R. & Krafft, C. Raman spectroscopic imaging for in vivo detection of cerebral brain metastases. *Anal. Bioanal. Chem.* **398**, 1707–1713 (2010).
  - [6] Krafft, C., Sobottka, S. B., Schackert, G. & Salzer, R. Raman and infrared spectroscopic mapping of human primary intracranial tumors: a comparative study. *J. Raman Spectrosc.* **37**, 367–375 (2006).
  - [7] Koljenović, S. *et al.* Discriminating vital tumor from necrotic tissue in human glioblastoma tissue samples by Raman spectroscopy. *Lab. Invest.* **82**, 1265–1277 (2002).
  - [8] Nijssen, A. *et al.* Discriminating basal cell carcinoma from its surrounding tissue by Raman spectroscopy. *J. Invest. Dermatol.* **119**, 64–69 (2002).
  - [9] Zumbusch, A., Holtom, G. & Xie, X. S. Three-dimensional vibrational imaging by coherent anti-Stokes Raman scattering. *Phys. Rev. Lett.* **82**, 4142–4145 (1999).
  - [10] Freudiger, C. W. *et al.* Label-free biomedical imaging with high sensitivity by stimulated Raman scattering microscopy. *Science* **322**, 1857–1861 (2008).
  - [11] Ozeki, Y., Dake, F., Kajiyama, S., Fukui, K. & Itoh, K. Analysis and experimental assessment of the sensitivity of stimulated Raman scattering microscopy. *Opt. Express* **17**, 3651–3658 (2009).
  - [12] Evans, C. L. *et al.* Chemical imaging of tissue in vivo with video-rate coherent anti-Stokes Raman scattering microscopy. *P. Natl. Acad. Sci. USA* **102**, 16807–16812 (2005).
  - [13] Saar, B. G. *et al.* Video-rate molecular imaging in vivo with stimulated Raman scattering. *Science* **330**, 1368–1370 (2010).
  - [14] Bachler, B. R., Fermann, M. E. & Ogilvie, J. P. Multiplex Raman induced Kerr effect microscopy. *Opt. Express* **20**, 835–844 (2012).
  - [15] Ploetz, E., Laimgruber, S., Berner, S., Zinth, W. & Gilch, P. Femtosecond stimulated Raman microscopy. *Appl. Phys. B* **87**, 389–393 (2007).
  - [16] Rock, W., Bonn, M. & Parekh, S. H. Near shot-noise limited hyperspectral stimulated Raman scattering spectroscopy using low energy lasers and a fast CMOS array. *Opt. Express* **21**, 15113–15120 (2013).
  - [17] Fu, D. *et al.* Quantitative chemical imaging with multiplex stimulated Raman scattering microscopy. *J. Am. Chem. Soc.* **134**, 3623–3626 (2012).
  - [18] Kong, L. *et al.* Multicolor stimulated Raman scattering microscopy with a rapidly tunable optical parametric oscillator. *Opt. Lett.* **38**, 145–147 (2013).
  - [19] Mueller, M. & Schins, J. M. Imaging the thermodynamic state of lipid membranes with multiplex CARS microscopy. *J. Phys. Chem. B* **106**, 3715–3723 (2002).

- [20] Cheng, J. X., Volkmer, A., Book, L. D. & Xie, X. S. Multiplex coherent anti-Stokes Raman scattering microspectroscopy and study of lipid vesicles. *J. Phys. Chem. B* **106**, 8493–8498 (2002).
- [21] Kano, H. & Hamaguchi, H. Femtosecond coherent anti-Stokes Raman scattering spectroscopy using supercontinuum generated from a photonic crystal fiber. *Appl. Phys. Lett.* **85**, 4298–4300 (2004).
- [22] Kee, T. W. & Cicerone, M. T. Simple approach to one-laser, broadband coherent anti-Stokes Raman scattering microscopy. *Opt. Lett.* **29**, 2701–2703 (2004).
- [23] Ploetz, E., Marx, B. & Gilch, P. Disturbing interference patterns in femtosecond stimulated Raman microscopy. *J. Raman Spectrosc.* **41**, 609–613 (2009).
- [24] Müller, M. & Zumbusch, A. Coherent anti-Stokes Raman scattering microscopy. *ChemPhysChem* **8**, 2156–2170 (2007).
- [25] Liu, Y., Lee, Y. J. & Cicerone, M. T. Broadband CARS spectral phase retrieval using a time-domain KramersKronig transform. *Opt. Lett.* **34**, 1363–1365 (2009).
- [26] Vartiainen, E. M. Phase retrieval approach for coherent anti-Stokes Raman scattering spectrum analysis. *J. Opt. Soc. Am. B* **9**, 1209–1214 (1992).
- [27] Cicerone, M. T., Aamer, K. A., Lee, Y. J. & Vartiainen, E. Maximum entropy and time-domain Kramers-Kronig phase retrieval approaches are functionally equivalent for CARS microspectroscopy. *J. Raman Spectrosc.* **43**, 637–643 (2012).
- [28] Pohling, C., Backup, T., Pagenstecher, A. & Motzkus, M. Chemoselective imaging of mouse brain tissue via multiplex CARS microscopy. *Biomed. Opt. Express* **2**, 2110–2116 (2011).
- [29] Parekh, S. H., Lee, Y. J., Aamer, K. A. & Cicerone, M. T. Label-free cellular imaging by broadband coherent anti-Stokes Raman scattering microscopy. *Biophys. J.* **99**, 2695–2704 (2010).
- [30] Lim, S. H., Caster, A. G., Nicolet, O. & Leone, S. R. Chemical imaging by single pulse interferometric coherent anti-stokes Raman scattering microscopy. *J. Phys. Chem. B* **110**, 5196–5204 (2006).
- [31] Dudovich, N., Oron, D. & Silberberg, Y. Single-pulse coherently controlled nonlinear Raman spectroscopy and microscopy. *Nature* **418**, 512–514 (2002).
- [32] Selm, R. *et al.* Ultrabroadband background-free coherent anti-Stokes Raman scattering microscopy based on a compact Er:fiber laser system. *Opt. Lett.* **35**, 3282–3284 (2010).
- [33] Ozeki, Y. *et al.* High-speed molecular spectral imaging of tissue with stimulated Raman scattering. *Nature Photon.* **6**, 845–851 (2012).
- [34] Deng, H., Bloomfield, V. A., Benevides, J. M. & Thomas, G. J. Dependence of the Raman signature of genomic B-DNA on nucleotide base sequence. *Biopolymers* **50**, 656–666 (1999).
- [35] Frushour, B. G. & Koenig, J. L. Raman scattering of collagen, gelatin, and elastin. *Biopolymers* **14**, 379–391 (1975).
- [36] Le, T. T., Langohr, I. M., Locker, M. J., Sturek, M. & Cheng, J. X. Label-free molecular imaging of atherosclerotic lesions using multimodal nonlinear optical microscopy. *J. Biomed. Opt.* **12**, 054007 (2007).
- [37] Zipfel, W. R. *et al.* Live tissue intrinsic emission microscopy using multiphoton-excited native fluorescence and second harmonic generation. *P. Natl. Acad. Sci. USA* **100**, 7075–7080 (2003).
- [38] Dong, R., Yan, X., Pang, X. & Liu, S. Temperature-dependent Raman spectra of collagen and DNA. *Spectrochim. Acta A* **60**, 557–561 (2004).
- [39] Sun, Y. *et al.* Investigating mechanisms of collagen thermal denaturation by high resolution second-harmonic generation imaging. *Biophys. J.* **91**, 2620–2625 (2006).
- [40] Fu, Y., Wang, H., Shi, R. & Cheng, J. X. Second harmonic and sum frequency generation imaging of fibrous astroglial filaments in ex vivo spinal tissues. *Biophys. J.* **92**, 3251–3259 (2007).
- [41] Theodossiou, T. *et al.* Thermally induced irreversible conformational changes in collagen probed by optical second harmonic generation and laser-induced fluorescence. *Lasers Med. Sci.* **17**, 34–41 (2002).
- [42] Krafft, C. *et al.* FTIR, Raman, and CARS microscopic imaging for histopathologic assessment of brain tumors. *Proc. SPIE* **7560**, 756007 (2010).
- [43] Wood, B. R. & McNaughton, D. Raman excitation wavelength investigation of single red blood cells in vivo. *J. Raman Spectrosc.* **33**, 517–523 (2002).
- [44] Yates, A. J., Thompson, D. K., Boesel, C. P., Albrightson, C. & Hart, R. W. Lipid composition of human neural tumors. *J. Lipid Res.* **20**, 428–436 (1979).
- [45] Krafft, C., Sobottka, S. B., Schackert, G. & Salzer, R. Analysis of human brain tissue, brain tumors and tumor cells by infrared spectroscopic mapping. *Analyst* **129**, 921–925 (2004).
- [46] Hartshorn, C. M. *et al.* Multicomponent chemical imaging of pharmaceutical solid dosage forms with broadband CARS microscopy. *Anal. Chem.* **85**, 8102–8111 (2013).

### Acknowledgments

The authors wish to thank Qiulian Wu, James Hale, and Maksim Sinyuk for preparing the pathological tissue specimens, and Stephanie Miller for preparation of neat chemical specimens. Additionally, C. H. Camp Jr., J. M. Heddleston, and C. M. Hartshorn wish to thank the National Research Council for support through the Research Associate Program (RAP). This work was supported in part by NIH/NIBIB grant 2P41EB001046-11.

### **Author contributions**

C.H.C. performed all experiments, analyzed all data, and drafted the manuscript. C.H.C. and M.T.C. designed all experiments and constructed the final manuscript. M.T.C. and Y.J.L. conceptualized the complimentary 2-colour/3-colour excitation scheme. C.H.C. constructed the instrument, modified the laser system, and developed the high-speed acquisition and processing software. C.H.C., Y.J.L., C.M.H., and M.T.C. developed signal processing methodology and protocols. M.T.C. developed the Kramers-Kronig transform and C.H.C. developed the parallelized, high-speed implementation. A.R.H.W., J.M.H., J.N.R., and J.D.L. provided materials and/or the tumour sections and provided histopathology insights and direction. J.M.H. assisted in performing the tumour section study, as well as contributing to the text of this manuscript. A.R.H.W., H.M.H., and C.H.C. collected the spontaneous Raman spectra of glycerol and C.H.C. performed the analysis. C.H.C. developed the presented mathematical framework of CARS generation and associated efficiencies with 2-/3-colour stimulation. M.T.C. supervised the study.

### **Additional information**

Correspondence and requests for materials should be addressed to M.T.C.

### **Competing financial interests**

The authors declare no competing financial interests.

Figure Legends

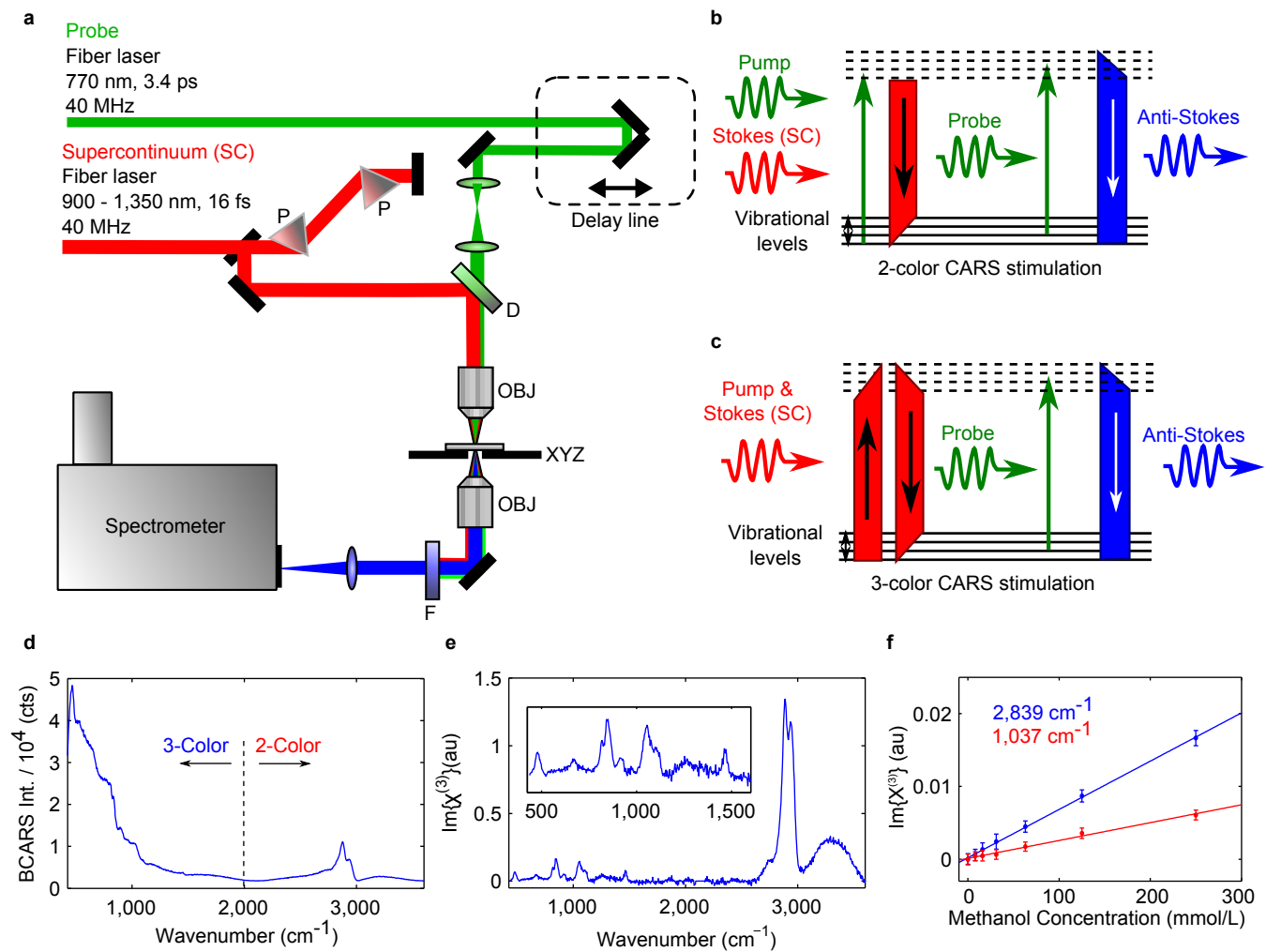


Figure 1: **Coherent Raman Imaging with BCARS microspectroscopy.** **a**, Schematic of the BCARS CRI system; P, SF10 prism; D, dichroic mirror; OBJ, objective lens; XYZ, piezoelectric stage; F, two short-pass filters. **b**, Energy diagram with 2-colour excitation. **c**, Energy diagram with 3-colour excitation. **d**, BCARS spectrum of 99 % glycerol at 3.5 ms exposure. **e**, Retrieved Raman spectrum of 99 % glycerol using the Kramers-Kronig transform. **f**, Linear dependence of the retrieved Raman spectrum on methanol concentration showing a detection limit of  $< 8$  mmol/L using the  $2,839 \text{ cm}^{-1}$  peak and  $< 28$  mmol/L using the  $1,037 \text{ cm}^{-1}$  peak. Error bars are  $\pm 1$  standard deviation.

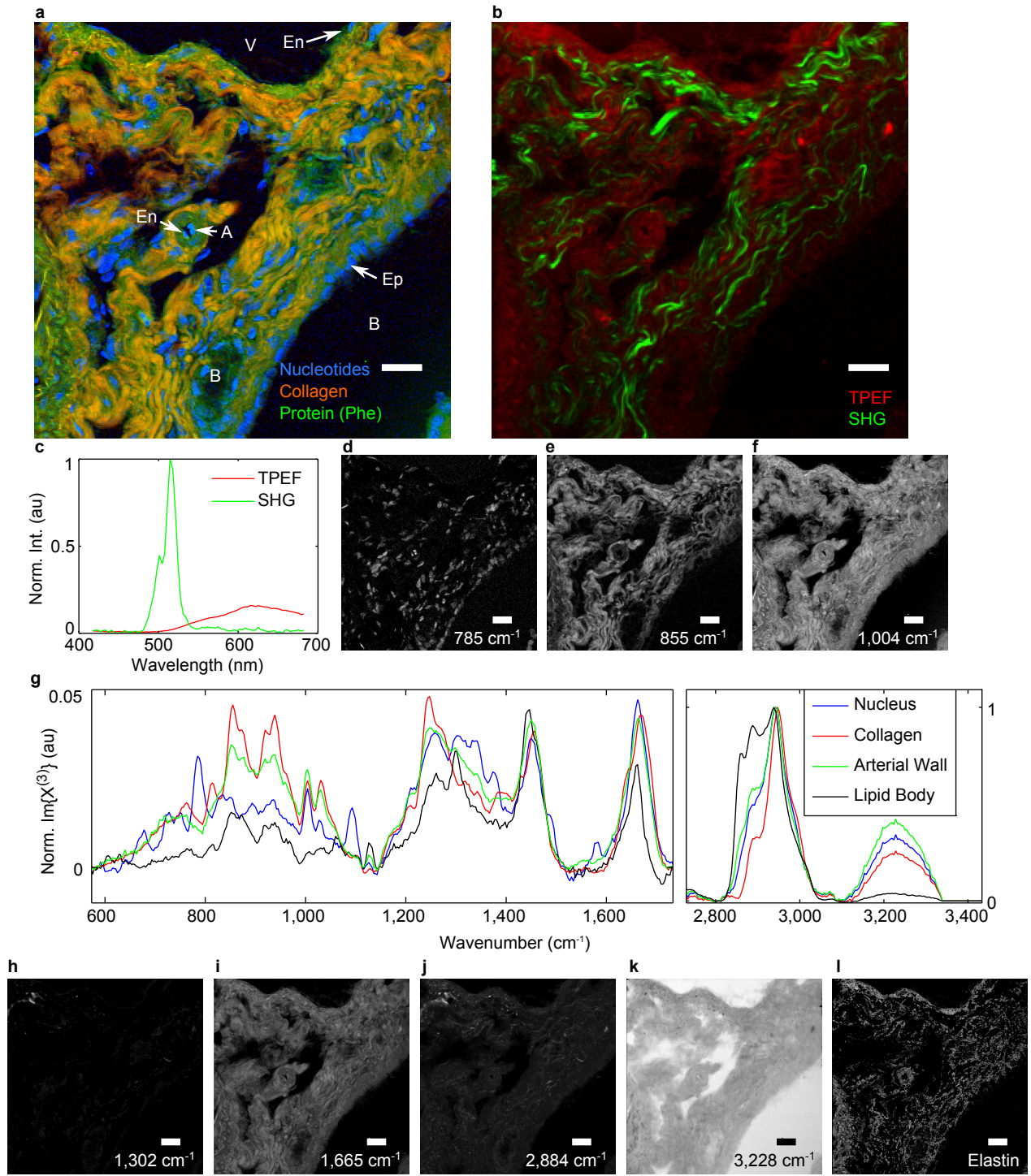


Figure 2: **CRI of murine liver tissue.** **a**, Spectral image of portal triad within murine liver tissue with the nuclei in blue, collagen in orange, and protein content in green. A, portal artery; B, bile duct; V, portal vein; Ep, epithelial cell; En, endothelial cell. **b**, SHG image highlighting the fibrous collagen network. **c**, SHG spectrum for a single pixel. **d-f**, Spectral images of individual vibrational modes represented by the colour channels in **a**: **d**, 785  $\text{cm}^{-1}$ ; **e**, 855  $\text{cm}^{-1}$ ; **f**, 1,004  $\text{cm}^{-1}$ . **g**, Single-pixel spectra from within the nucleus (DNA), collagen fiber, arterial wall, and a lipid droplet. **h-l**, Additional spectral channels that provide histochemical contrast: **h**, 1,302  $\text{cm}^{-1}$ ; **i**, 1,665  $\text{cm}^{-1}$ ; **j**, 2,884  $\text{cm}^{-1}$ ; **k**, 3,228  $\text{cm}^{-1}$ ; **l**, Elastin: (1,126 and 1,030)  $\text{cm}^{-1}$  but not (677, 817, and 1,302)  $\text{cm}^{-1}$ . Scale bars, 20  $\mu\text{m}$ .

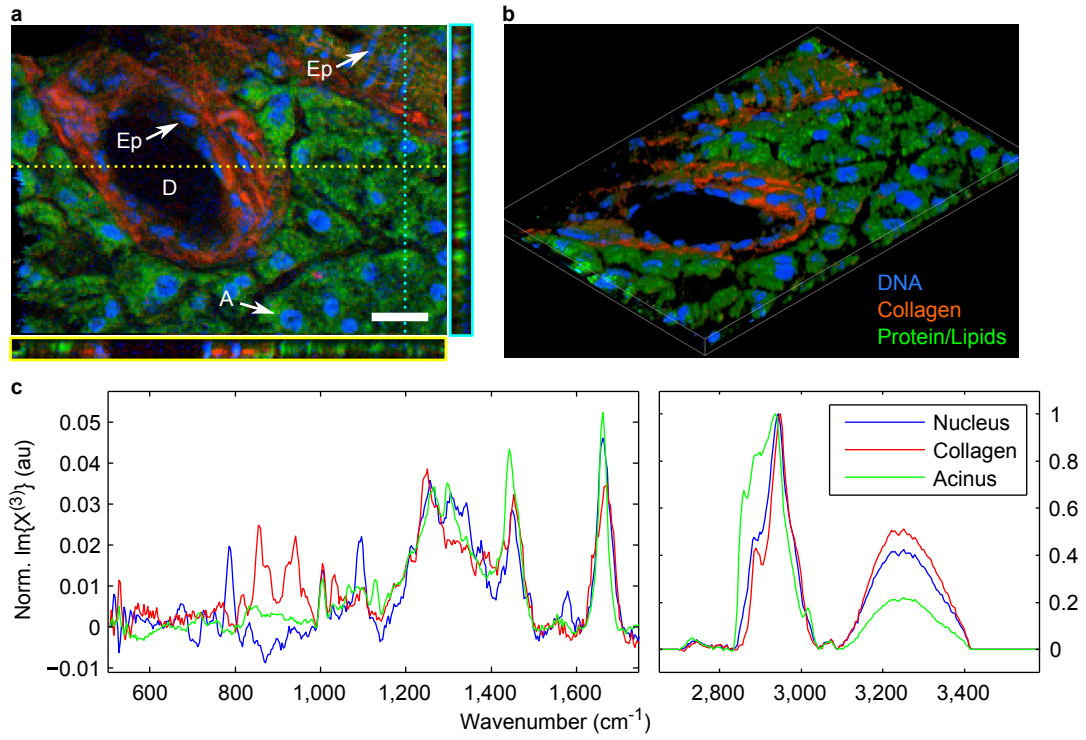


Figure 3: **Three-dimensional CRI of murine pancreatic ducts.** **a**, Pseudocolour image taken from a single plane of a Z-stack image collection of exocrine ducts highlighting nuclei ( $785\text{ cm}^{-1}$ ) in blue, collagen ( $855\text{ cm}^{-1}$ ) in red, and a composite of lipids and proteins in green ( $1,665\text{ cm}^{-1}$ ). D, exocrine duct; A, acinar cell; Ep, epithelial cell. Additionally, two axial planes are shown to provide histochemical depth information. **b**, Three-dimensional reconstruction of pancreatic ducts from 10 z-stack images. **c**, Single-pixel spectra taken from within an epithelial cell nucleus, within the fibrous collagen, and from within the cytosol of an acinar cell. Scale bar,  $20\text{ }\mu\text{m}$ .

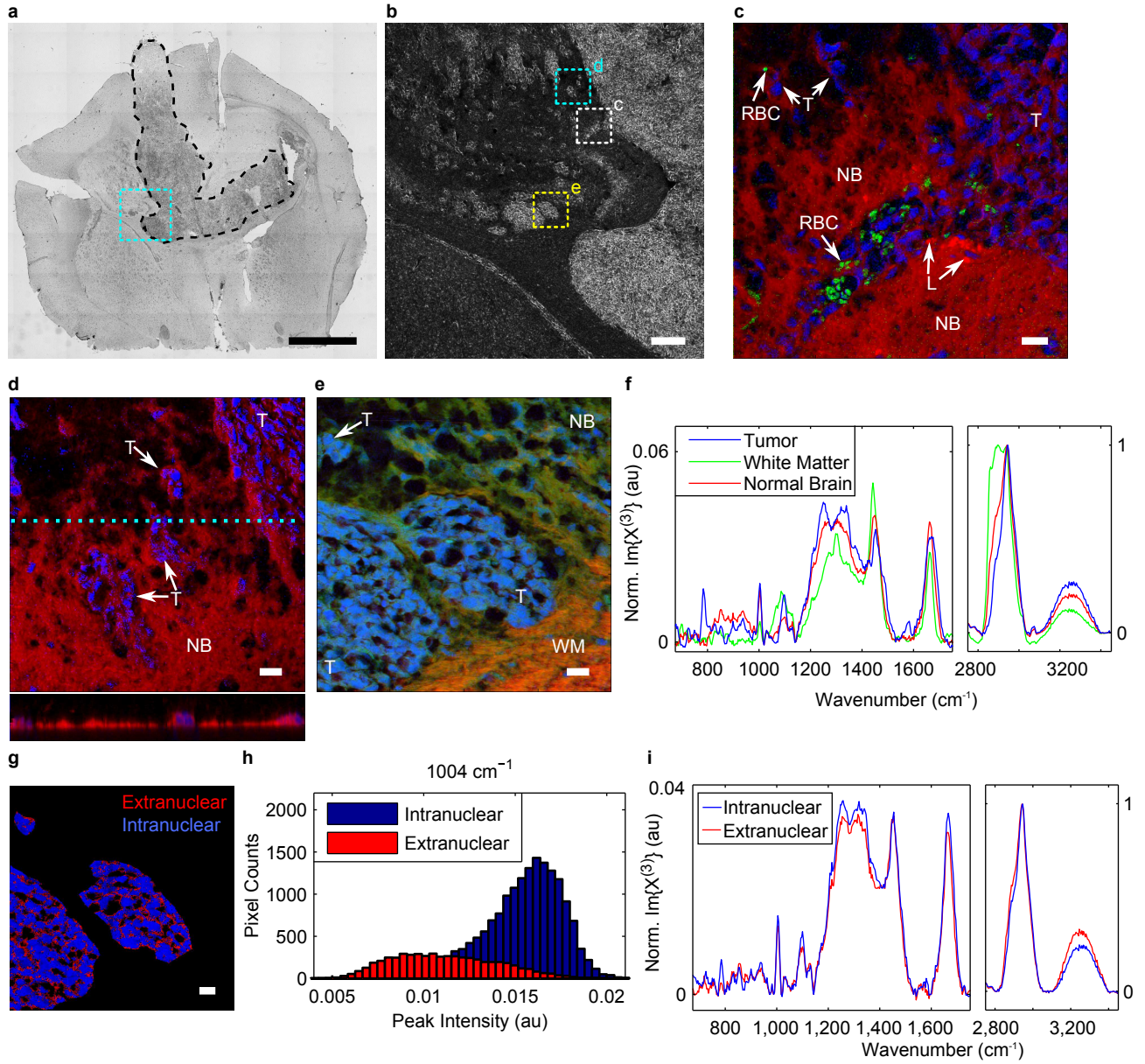


Figure 4: **Histopathology using broadband CRI.** **a**, Brightfield image of xenograft glioblastoma in mouse brain outlining tumour hard boundary (black, dashed line). Cyan dashed box indicates region of interest (ROI). Scale bar, 2 mm. **b**, Phase contrast micrograph of BCARS ROIs with boxes and associated subfigure labels. Scale bar, 200  $\mu\text{m}$ . **c**, Pseudocolour BCARS image of tumour and normal brain tissue highlighting nuclei (blue), lipid content (red), and red blood cells (green). **d**, BCARS image and axial scan highlighting nuclei (blue) and lipid content (red). **e**, BCARS image highlighting nuclei (blue), lipid content (red), and  $\text{CH}_3$ -stretch -  $\text{CH}_2$ -stretch (green). NB, normal brain; T, tumour cells; RBC, red blood cells; L, lipid bodies; WM, white matter. **f**, Single-pixel spectra. **g**, Spectrally segmented image of internuclear (blue) and extranuclear (red) tumoural spaces. **h**, Histogram analysis of phenylalanine content. **i**, Mean spectra from within tumour mass. **c - e & g**, Scale bars, 20  $\mu\text{m}$ .